

# Large-Scale Advanced Propeller Blade Pressure Distributions: Prediction and Data

N. Nallasamy,\* O. Yamamoto,† and S. Warsi‡  
*Sverdrup Technology, Inc., Brook Park, Ohio 44142*  
 and  
 L. J. Bober§  
*NASA Lewis Research Center, Cleveland, Ohio 44135*

Two Euler analysis techniques, finite difference and finite volume, were employed to predict the blade surface pressure distributions of a large-scale advanced propeller. The predicted pressure distributions were compared with wind-tunnel data. Both techniques produced blade pressure distributions that were in fairly good agreement with the data over the range of test Mach numbers of 0.2–0.78. However, the numerical simulations failed to predict correctly the measured pressure distributions for the low Mach number, high-power case. The data indicate the presence of a leading-edge vortex for this case. A discussion of the compressibility effects is also presented.

## Introduction

ADVANCED propellers employ highly loaded, highly swept, thin blades with variable pitch to achieve a higher propulsive efficiency than is achieved by the current high-bypass turbofans. Model tests have been carried out in wind tunnels and in flight to understand the aerodynamics and acoustics of the advanced designs. The propeller blade flows are complicated and involve a wide range of flow regimes, such as 1) takeoff conditions, where leading edge and tip vortices influence the performance and noise generation; and 2) cruise conditions, where shock waves add to the complexity. An understanding of the complex advanced propeller blade flows is essential for improving the current design methodologies.

Scale-model tests have provided integrated performance data. To obtain aerodynamic blade data, a series of tests on a large-scale, 9-ft, single-rotation SR7L propeller were conducted in a transonic wind tunnel in Modane, France. The tests were performed in the wind tunnel's 47-m<sup>2</sup> (506-ft<sup>2</sup>) transonic test section. The propfan was operated in two-bladed configuration (Fig. 1). This configuration was adopted for the tests because the drive power was insufficient for the eight-bladed propeller. The design characteristics of the SR7L propeller are given in Table 1.

The blade surface pressure was measured on a specially designed, pressure-tapped SR7L blade. There were 13 radial stations of pressure taps on each surface of the blade: 16 pressure taps were distributed along the blade chord at each radial station on the pressure (face) side and 20 were distributed on the suction (camber) surface. The taps were concentrated on the blade surface in the areas where large pressure gradients were expected. Each chordwise distribution was

aligned approximately with the expected streamline on the blade at the design cruise condition (Fig. 2). The blade surface pressures were recorded one radial station at a time, and the tests were conducted over the Mach number range of 0.03–0.78. A description of the nature and extent of the large-scale advanced propeller wind-tunnel tests is given by Campbell et al.<sup>1</sup>

The purpose of the present investigation is to evaluate the ability of the Euler analysis techniques to predict the blade

Table 1 SR7L propeller design parameters

Disk loading, kW/m <sup>2</sup> (shp/diam <sup>2</sup> )	259.6 (32)
Tip speed, m/s (ft/s)	243.8 (800)
Tip diameter, m (ft)	2.743 (9)
Hub-to-tip ratio	0.24
Advance ratio	3.06
Power coefficient	1.448
Integrated design lift coefficient	0.191
Blade tip sweep, deg	36
Number of blades	8

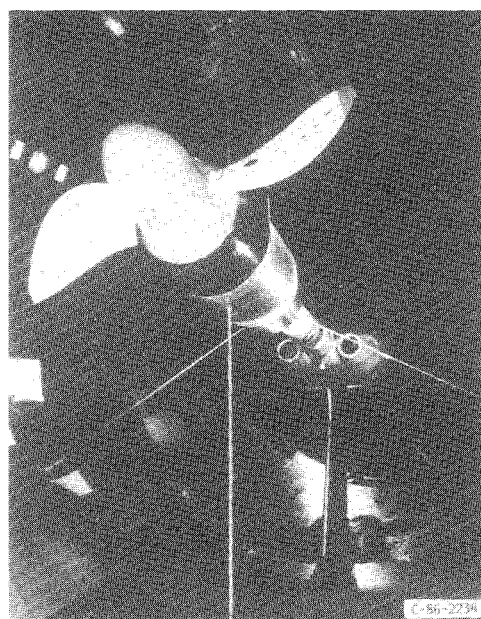


Fig. 1 SR7L propfan installed in the S1-MA transonic test section.

Presented as Paper 89-2696 at the AIAA/ASME/SAE/ASEE 25th Joint Propulsion Conference, Monterey, CA, July 10–12, 1989; received July 24, 1989; revision received Feb. 5, 1990. Copyright © 1990 by the American Institute of Aeronautics and Astronautics, Inc. No copyright is asserted in the United States under Title 17, U.S. Code. The U.S. Government has a royalty-free license to exercise all rights under the copyright claimed herein for Governmental purposes. All other rights are reserved by the copyright owner.

\*Senior Supervisor, Aeromechanics Department.

†Senior Research Engineer.

‡Research Engineer.

§Chief, Turbomachinery Technology Branch, Propulsion Systems Division.

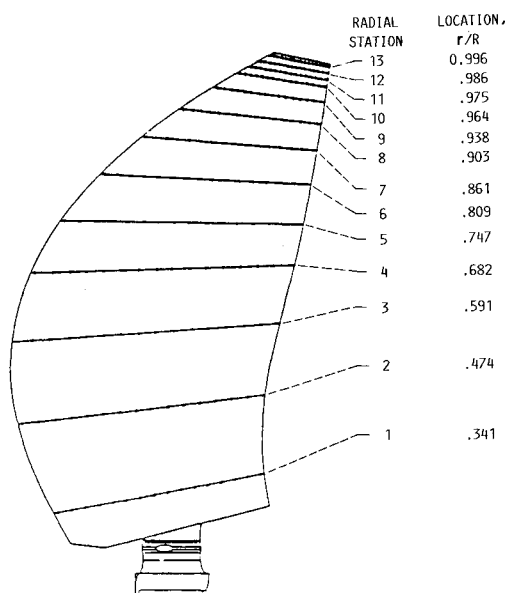


Fig. 2 Pressure tap locations.

surface pressure distributions. The three-dimensional Euler equations are solved by two different analysis techniques: 1) a finite difference technique (NASPROP) originally developed by Bober et al.<sup>2</sup> and 2) a finite volume technique developed by Denton.<sup>3</sup> In this article, the predicted chordwise pressure distributions and the integrated power coefficients are compared with the test data for the Mach number range from 0.2 to 0.78.

### Computational Methods

Two numerical codes are employed to simulate the flowfield about the two-bladed, single-rotation propeller (SR7L) subject to conditions prescribed in the Modane, France test. Both codes use an asymptotic time-marching approach to obtain the steady-state solutions of the three-dimensional Euler equations governing the propeller flow. Brief descriptions of each code follow.

### Finite Difference Euler Solver

The finite difference Euler solver (NASPROP) was originally developed by Bober et al.<sup>2</sup> Their three-dimensional Euler analysis was the first to provide detailed solutions of the advanced propeller flowfield. Since then the code has been rewritten incorporating improved boundary conditions and has been vectorized for the CRAY computer.

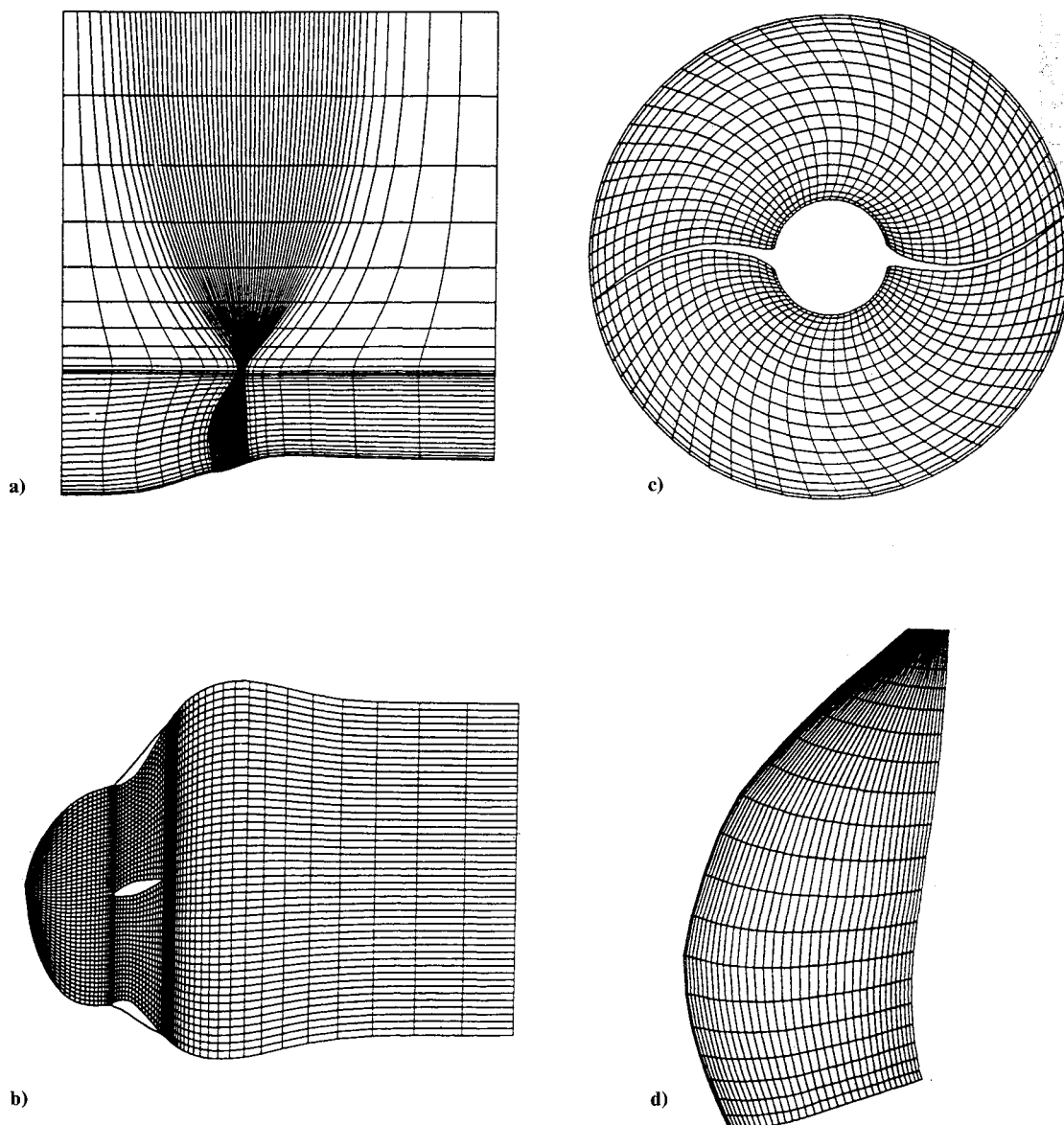


Fig. 3 Typical computational grid: a) bladewise surface; b) streamwise surface; c) spanwise surface; and d) distribution of grid points on the blade surface.

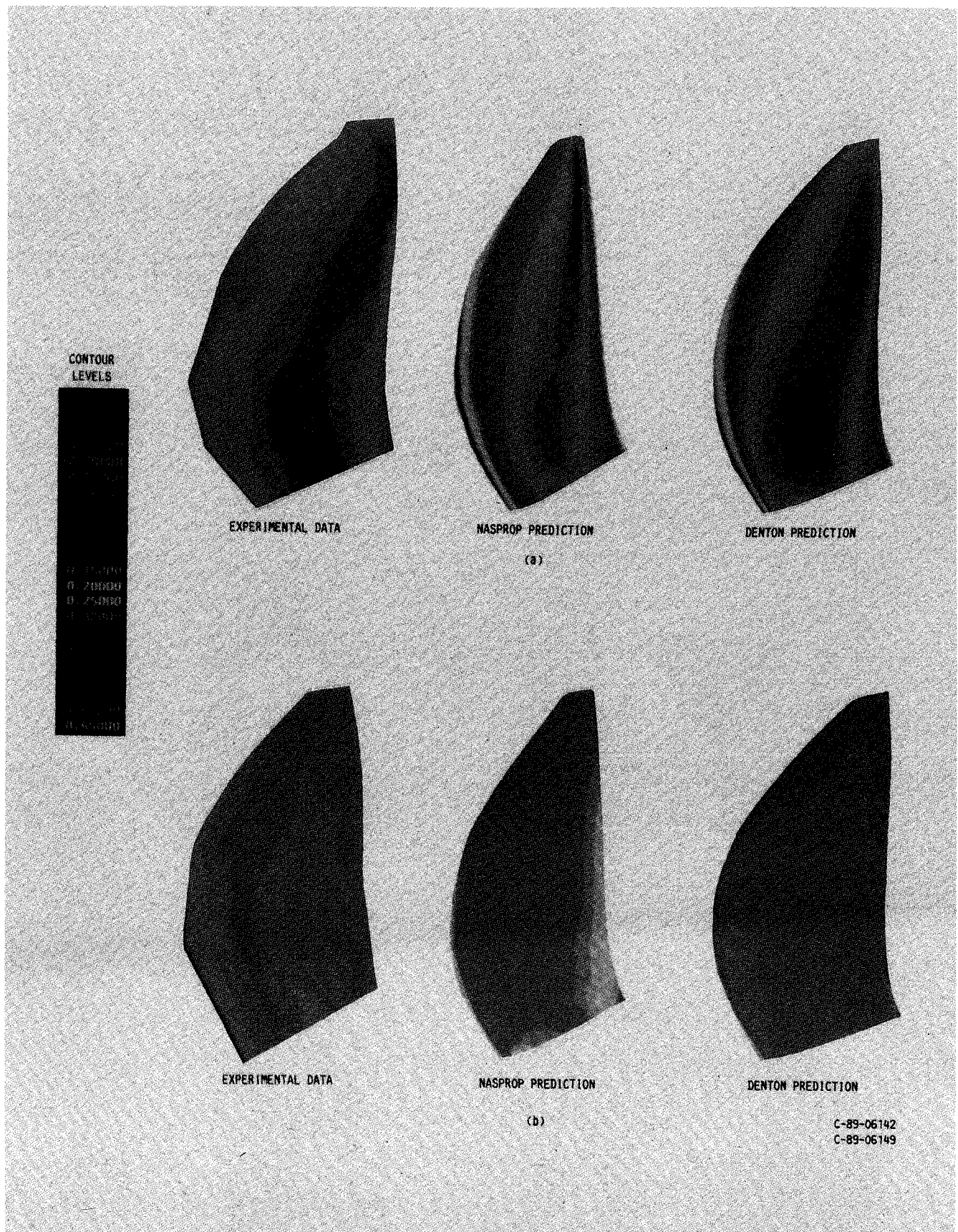


Fig. 4 Comparison of predicted and measured pressure coefficient distributions for test 12 (Mach 0.775): a) suction surface; and b) pressure surface.

The Euler equations, in conservative differential form, are transformed from a cylindrical coordinate system to a time-dependent, body-fitted, curvilinear reference frame. The transformed equations are treated as a system of coupled first-order, autonomous differential equations. The equations are cast in nondimensional form. First-order-accurate implicit Euler time differencing is employed, and the flux vectors are linearized by Taylor series expansion up to second order in time. The spatial derivatives are replaced by central differences with appropriate one-sided differences at the boundaries. The resulting implicit operators involve inversions of a block tridiagonal system. The system can be reduced to scalar tridiagonal matrices by applying a diagonalization technique<sup>4</sup> to the flux Jacobian matrices. Constant coefficient, second-order implicit, and fourth-order explicit dissipation terms are added for stability considerations. A periodic tridiagonal matrix inversion is employed in the circumferential direction. Further details of the solution procedure and the implementation of the boundary conditions can be found in Refs. 5 and 6.

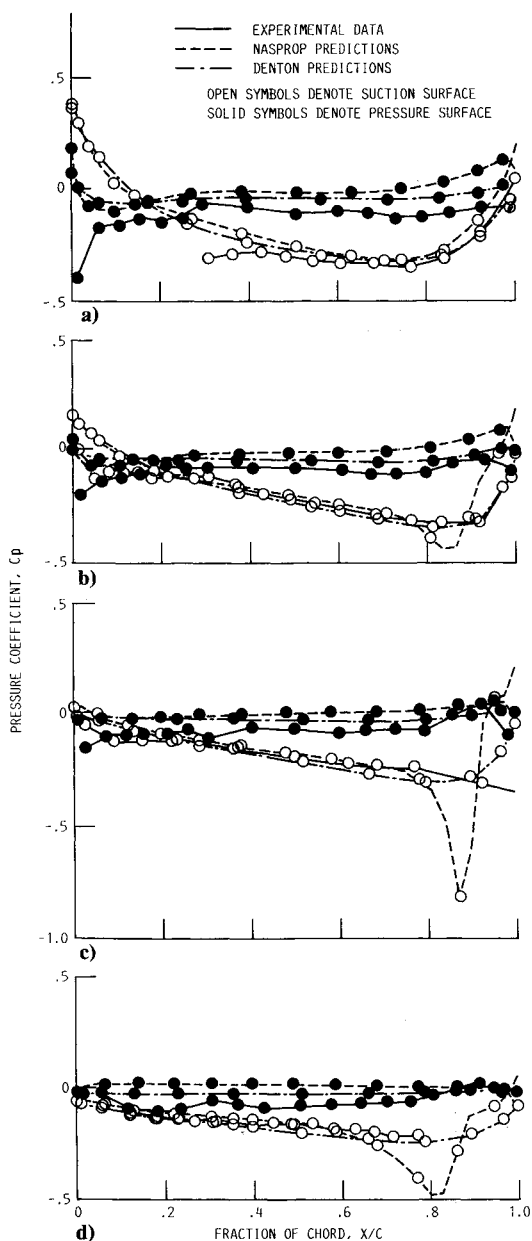


Fig. 5 Chordwise distribution of pressure coefficients for test 12 (Mach 0.775): a) radial location,  $r/R = 0.569$ ; b) radial location,  $r/R = 0.739$ ; c) radial location,  $r/R = 0.862$ ; and d) radial location,  $r/R = 0.975$ .

### Finite Volume Euler Solver

The finite volume Euler solver was originally developed by Denton for the analysis of turbomachinery flows<sup>3</sup> and was later modified to compute the advanced propeller flowfield.<sup>7,8</sup> In Denton's analysis, the three-dimensional Euler equations are written in a coordinate frame rotating with the blade. The governing equations are solved in the physical domain on a grid that is generated algebraically. The flow domain is discretized by using three kinds of surfaces: the bladewise surface, streamwise surface, and spanwise surface. The computational nodes are located at the corners of each volume element. The fluxes of mass, momenta, and energy through each face are calculated by using the averages of flow properties stored at the corners of that face.

Denton's explicit time-marching method employs an opposed difference scheme. The scheme uses upwind differences for fluxes of mass and momenta and downwind differences for pressure in the streamwise direction. The derivatives in the circumferential direction are evaluated by using central differences. The time-marching method uses a time step such that the Courant number is close to unity. The method itself ensures stability by solving the flow equations in the order of continuity, energy, and momentum. A variable time step ap-

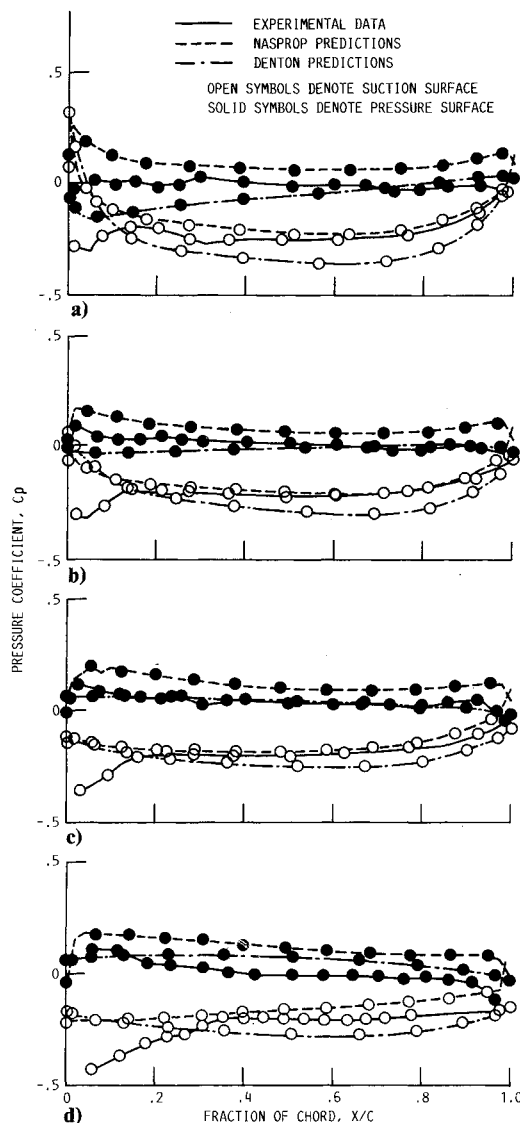


Fig. 6 Chordwise distribution of pressure coefficients for test 8 (Mach 0.5): a) radial location,  $r/R = 0.569$ ; b) radial location,  $r/R = 0.739$ ; c) radial location,  $r/R = 0.862$ ; and d) radial location,  $r/R = 0.975$ .

appropriate for each volume element is used to accelerate convergence. The method is of first-order accuracy and is modified to achieve greater accuracy by adding a lagged correction factor to correct the downwind pressure. A smoothing factor is used after each time step to smooth out any waviness in the circumferential direction. The convergence is judged on the basis of mass conservation and the maximum change in the axial velocity component. Further details of the solution procedure and the implementation of the boundary conditions can be found in Refs. 3 and 8.

### Computational Grid

In this article, the steady-state propeller flowfield with the propeller axis at zero angle of attack is computed. Hence, only one blade passage needs to be considered as a computational domain since the flowfield is periodic in the blade-to-blade direction.

The computational domain is discretized by three type of surfaces. The bladewise surfaces are bounded by two planes—one plane containing the suction side of one blade and the other plane containing the pressure side of the adjacent blade (Fig. 3a). The surfaces are clustered near the blades, and larger spacings are used between the blades. The streamwise surfaces

(Fig. 3b) are placed in the radial direction and are limited by the spinner-nacelle surface and the far-field boundary. The far-field boundary is placed at two blade radii beyond the blade tip. Small spacings are used in the blade tip region to capture the tip vortex flow. The spanwise surfaces are bounded by inlet and exit planes in the axial direction (Fig. 3c). The inlet plane is placed at one radius upstream of the spinner, and the exit plane is located three radii behind the blade. Grid points are clustered near the leading and trailing edges.

From a few grid-sensitivity calculations, 35 chordwise and 20 spanwise points on each side of the blade are found to be adequate to obtain a solution that is nearly independent of the grid. Figure 3d shows the distribution of grid points on the blade surface. A total of  $61 \times 33 \times 35$  (axial, radial, and circumferential) grid points is used to discretize the whole computational space. The same grid density on the blade surfaces, and similar grid arrangements, are employed by the two computer programs.

### Results and Discussion

The steady three-dimensional flowfield of an advanced propeller, SR7L, is considered here. The Euler equations governing the flowfield are solved by a finite difference and a finite volume technique. The numerical results are compared with wind-tunnel data.

The numerical data for nine of the Modane test cases (Table 2) were generated by the two numerical codes independently. Although each code used its own grid generator for high Mach number runs, both used the same grid generator for low Mach number (0.2) runs. The results are compared with the wind-tunnel data in the form of surface pressure contours, chordwise pressure distributions, and total power coefficients.

The pressure coefficient is defined in this paper as

$$C_p = \sum_{ij} \frac{P_{ij} - P_\infty}{0.5 \rho_\infty (V_\infty^2 + r_{ij}^2 \omega^2)}$$

where  $P_{ij}$  and  $r_{ij}$  are the local pressure and radial distance to the data point, respectively;  $P_\infty$ ,  $\rho_\infty$ , and  $V_\infty$  are the pressure, density, and velocity of the freestream, respectively and  $\omega$  is the rotational speed (rad/s) of the blade. The computed pressure is interpolated to match the radial location of the pressure taps. The total power coefficient of the propeller is computed from the blade surface pressure by

$$CP = \sum_{ij} \frac{2\pi}{\rho_\infty \Omega^2 D^5} r_{ij} (P_{ij} \Delta A_{ij})_\Theta B$$

where  $\Delta A_{ij}$  is the elemental surface area formed by four neighboring grid points,  $r_{ij}$  the radial distance of the element,  $D$  the diameter of the propeller,  $\Omega$  the rotational velocity (rev/s), and  $B$  the number of blades. The subscript  $\Theta$  denotes the component in the tangential direction.

The Modane test results<sup>9</sup> and the computed power coefficients are presented in Table 2. The Mach number and the advance ratio for the computations were matched with the experimental conditions. The use of nominal blade setting angles for computations resulted in power coefficients higher than the measured ones. Based on the computed power coefficients, a second set of blade setting angles were chosen within the tolerance limits to make the predictions closer to the data. These blade setting angles, which were used in the computations, and the resulting power coefficients are given in Table 2. For high Mach number tests, the power coefficients are still overpredicted. The blade setting angles may have to be lowered beyond the tolerance limits to improve the agreement in these cases. No further change in the blade setting angle was made.

The power coefficients predicted by the numerical codes closely follow the power trends that are observed in the experiments. Tests 5 and 6 are designed to compare the power at cutback and takeoff conditions at low Mach number. The

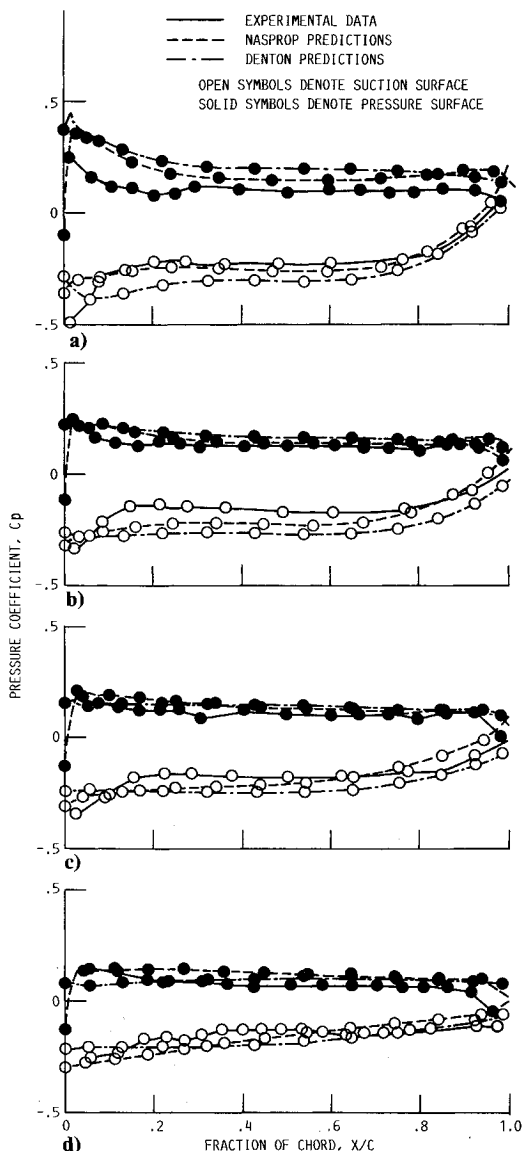


Fig. 7 Chordwise distribution of pressure coefficients for test 5 (Mach 0.2): a) radial location,  $r/R=0.569$ ; b) radial location,  $r/R=0.739$ ; c) radial location,  $r/R=0.862$ ; and d) radial location,  $r/R=0.975$ .

predictions show the correct trend, except that the NASPROP code underpredicts the measured value in test 6.

Tests 7, 8, and 9 show the power trend when the blade angle is changed and the Mach number and the advance ratio are kept constant. For low-power range, NASPROP results show excellent agreement with the wind-tunnel data.

Tests 10-12 are designed to show the Mach number effect when the blade angle is kept constant. Through these tests, the power stays relatively constant, although the results of the finite difference code show a slight increase with Mach number. The Denton code results show nearly the same trend as the data. The last test was conducted as a variation of test 12 with a different advance ratio. The inverse relation between the power coefficient and the advance ratio is predicted correctly by both numerical codes; however, the finite difference code tends to overpredict the power consistently for these cases.

Three representative test cases were chosen for detailed comparisons: test 12 for a high Mach number (0.775), test 8 for an intermediate Mach number (0.5), and test 5 for a low Mach number (takeoff, 0.2).

Contours of measured surface pressure for test 12 are shown in Figs. 4. Because of the coarseness of the experimental data points, the blade shape and the contour lines are not smoothly constructed. Although there are 20 pressure taps in each of the 13 radial stations on the suction side and 16 taps on each pressure surface radial station, data were recorded for only 10 radial stations for test 12. Also, a few pressures were not valid at several radial stations. Missing data were approximated by interpolation or extrapolation from neighboring data. It should be noted that the blade outline in the test data is based on the pressure tap locations and does not represent the true outline of the blade.

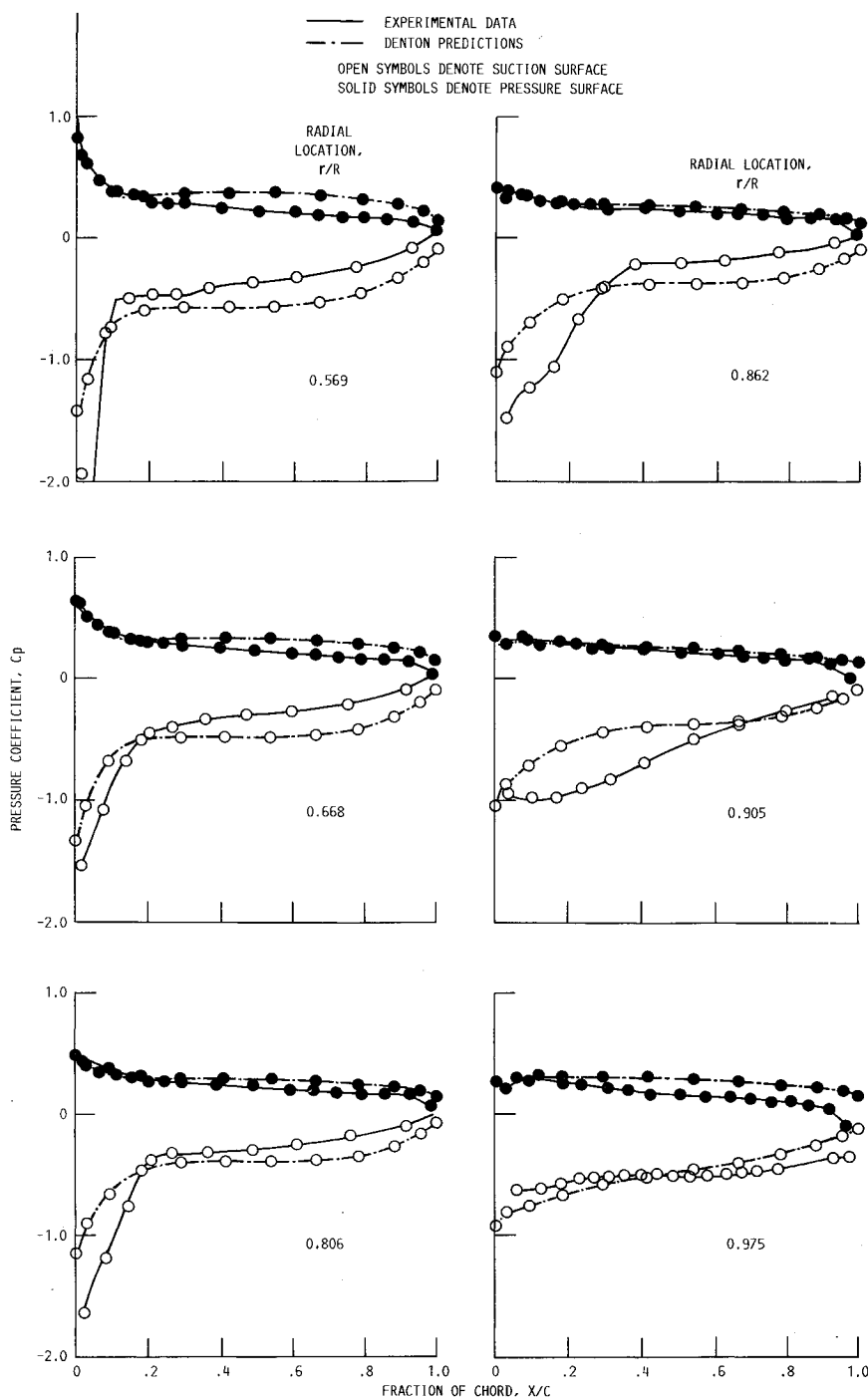


Fig. 8 Comparison of predicted and measured pressure coefficients for test 6 (Mach 0.2).



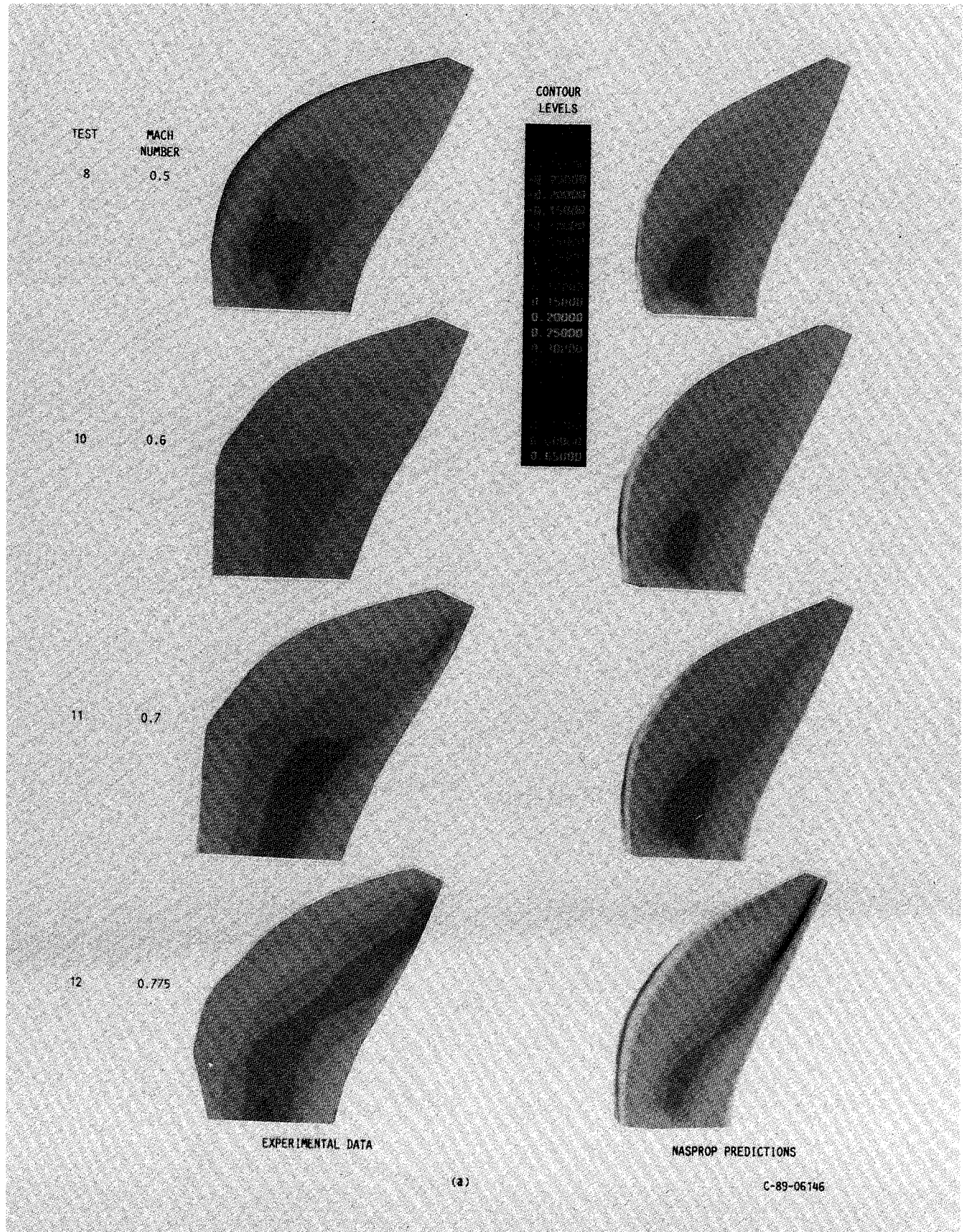


Fig. 9 Comparison of predicted and measured compressibility effects—pressure coefficient distributions for various Mach numbers: a) suction surface; and b) pressure surface.



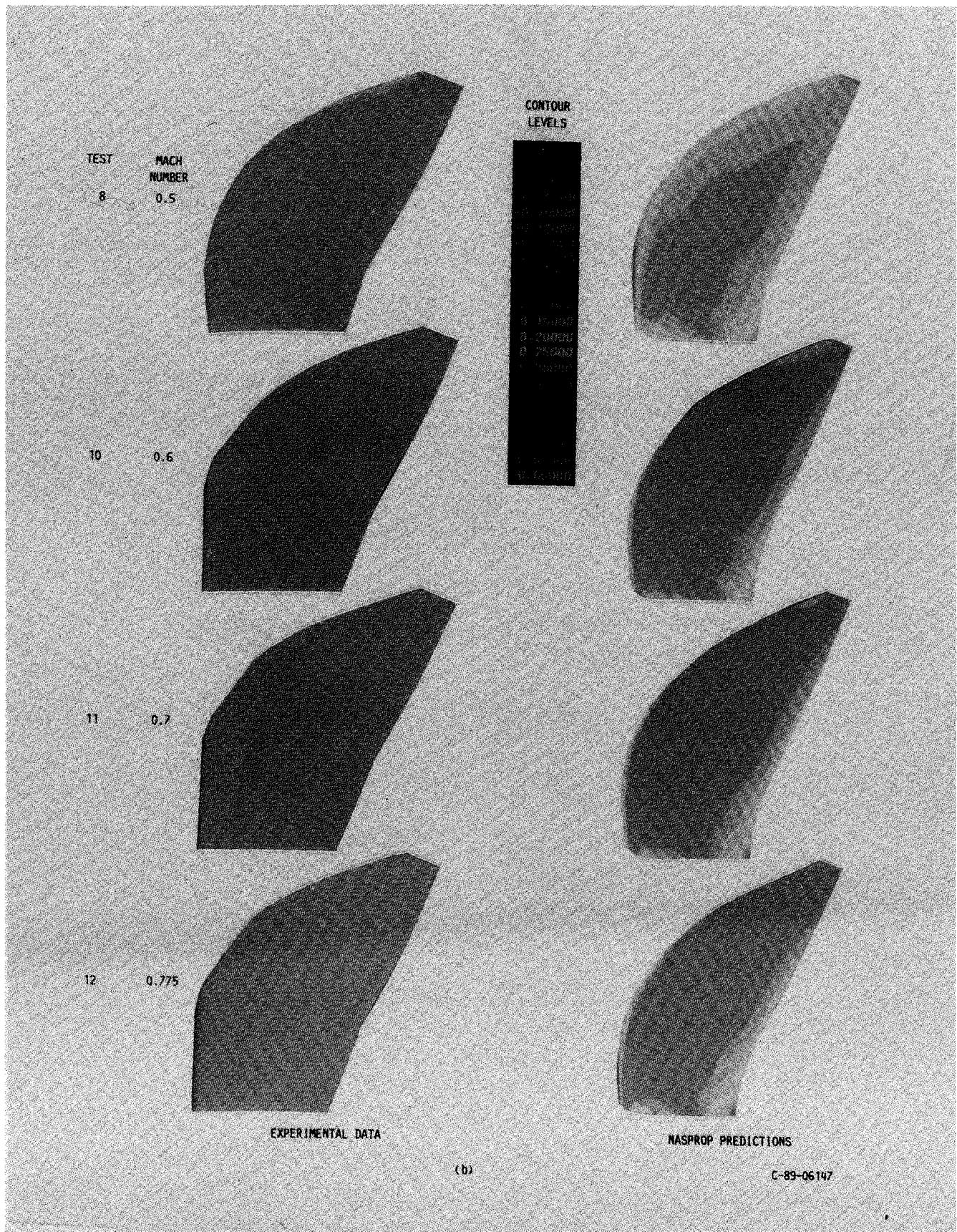


Fig. 9 (continued) Comparison of predicted and measured compressibility effects—pressure coefficient distributions for various Mach numbers: a) suction surface; and b) pressure surface.



The corresponding data generated by the two numerical codes are also shown in Figs. 4. Similarity between the numerical results is clearly seen. On the suction side (Fig. 4a), the contour features can be identified easily with those of the data. The agreement of the predictions with the data on the pressure surface (Fig. 4b) is not as good as that on the suction surface.

Detailed chordwise pressure distributions at four radial stations ( $r/R = 0.569, 0.739, 0.862$ , and  $0.975$ ) are shown in Figs. 5a-d, respectively. Better agreement is seen on the suction side, except that a strong shock is generated at the outboard trailing edge by the NASPROP code.

Contrary to the NASPROP results, the Denton code does not show the formation of a strong shock though it clearly shows the compressibility effect in the region and agrees well with the measurements. Both tend to overpredict the pressures on the pressure side, which is reflected in the power coefficient comparison in Table 2. The inverted loading near the leading-edge region obtained in the data is predicted poorly on the inboard region. This may be the result of the leading-edge geometry represented by the numerical codes not exactly matching the physical blade geometry. The estimated structural deflections at the design point cruise condition were used for all of the runs.

The local chordwise pressure distributions at the four radial stations for test 8 are compared with test data in Figs. 6. Chordwise pressure profiles reveal that the loading is distributed fairly evenly from the hub to the tip at this condition. Both codes show reasonably good agreement at all four radial stations. The pressure side is predicted better by the Denton code than by the NASPROP code. In general, better agreements are seen in the outboard section of the blade, and discrepancies are observed at the inboard leading-edge section.

Numerical results are compared with experimental data (test 5, Mach 0.2) in Figs. 7. The figures show that both numerical predictions agree very well with test data, especially in the outboard section of the blade. The Denton code slightly overpredicted the pressure loading throughout the blade, which resulted in a power coefficient that was higher than the experimental value (Table 2).

Figures 8 show a low Mach number case (Mach 0.2, test 6) with a higher power and present an interesting flow phenomenon. The numerical results are represented by the Denton calculations. The code is able to capture the high-pressure loading at the leading edge reasonably well. The wind-tunnel data show broadening of the suction peak on the suction side at radial stations  $r/R = 0.862$  and  $0.905$ . This behavior of the

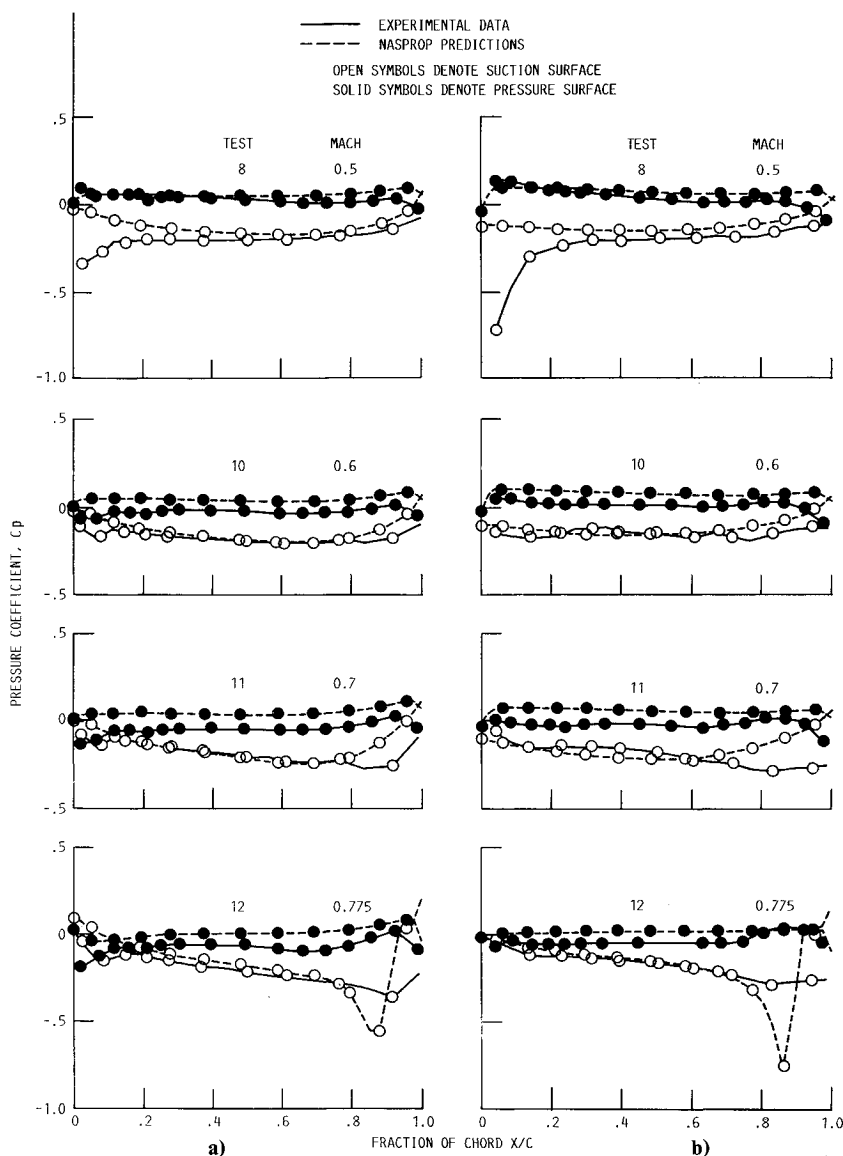


Fig. 10 Comparison of predicted and measured compressibility effects—chordwise distribution of pressure coefficients for two radial locations for various Mach numbers: a) radial location,  $r/R = 0.8060$ ; and b) radial location,  $r/R = 0.9390$ .

Table 2 Modane test operating conditions

Test number	Mach number	Advance ratio	Blade angle, deg		Power coefficient		
			Test	Calculation	Test	NASPROP calculation	Denton calculation
5	0.2	0.88	26.6 ± 1.0	25.6	0.100 ± 0.002	0.108	0.121
6	0.2	0.883	31.3 ± 0.9	30.4	0.250 ± 0.001	0.193	0.283
7	0.5	3.083	58.5 ± 1.0	57.5	0.642 ± 0.009	0.564	0.692
8	0.5	3.067	55.1 ± 0.8	55.0	0.361 ± 0.005	0.369	0.344
9	0.5	3.071	51.8 ± 0.9	51.6	0.110 ± 0.004	0.106	0.112
10	0.6	3.078	54.5 ± 1.3	53.6	0.230 ± 0.006	0.254	0.262
11	0.7	3.064	54.5 ± 1.3	53.6	0.228 ± 0.006	0.271	0.244
12	0.775	3.088	54.5 ± 1.3	53.6	0.227 ± 0.003	0.286	0.247
13	0.78	3.209	54.5 ± 1.3	53.6	0.111 ± 0.005	0.207	0.134

pressure curve is considered to be the result of the formation of a leading-edge vortex. Oil flow studies of surface streamlines indicate the formation of such leading-edge vortices.<sup>10,11</sup> Unfortunately, with the conditions prescribed in the Modane test and the grid distribution employed in the present numerical solutions, the vortex flow has not been captured by either numerical code. Grid refinement and improved dissipation models may be necessary to predict the leading-edge vortex. Numerical solutions of the Euler equations have been found to predict the leading-edge vortices on swept wings fairly well.<sup>12</sup>

Finally, the Mach number effect is demonstrated in Figs. 9 and 10. Figure 9a shows the NASPROP pressure contours on the suction side for four Mach numbers, 0.5, 0.6, 0.7, and 0.775 (tests 8 and 10–12, respectively) and the corresponding experimental data. The pressure surface predictions are compared with data in Fig. 9b. It should be noted that for this compressibility study the blade angle is kept constant. However, for the experimental results, a slightly different blade angle was used for the Mach 0.5 case (see Table 2). With increasing Mach number, more significant changes in the flow occur on the suction side than on the pressure side. The predicted flow features compare well with the experimental data.

Figures 10 show the local pressure distributions at two outboard stations,  $r/R = 0.806$  and  $0.939$ , for the compressibility study. Although no significant changes are observed for low Mach number, the evidence of a compression wave starts to develop on the suction side when the Mach number reaches about 0.7. A freestream Mach number of 0.78, the compression wave fully develops to a trailing-edge shock. The NASPROP results agree with the experimental data up to the development of the compression wave. However, the strong trailing-edge shock formation is not indicated by the test data or the results of the Denton code. The reasons for this discrepancy are not clear.

### Concluding Remarks

The detailed chordwise pressure distributions of an advanced propeller were predicted by two numerical techniques of solving the three-dimensional Euler equations, finite difference and finite volume, and were compared with wind-tunnel data. In general, both techniques predicted the blade surface pressure distributions fairly well for the range of Mach numbers considered (0.2–0.78). The strong trailing-edge shock predicted by the finite difference code (NASPROP) at high Mach numbers (0.775 and 0.78) was not observed either in the exper-

imental data or in the Denton code predictions. In the intermediate Mach number range (0.5–0.7), the agreement of the predictions with data was good. Generally, the predictions showed better agreement at the outboard section than at the inboard section. For the low Mach number (0.2) cases, the agreement of the predictions with data was best for the low-power case. The data for the high-power case seem to show the formation of a leading-edge vortex that is not captured by the numerical techniques. Grid refinement and improved dissipation models may be required to capture the leading-edge vortex.

### References

- <sup>1</sup>Campbell, W. A., Wainauski, H. S., and Bushnell, P. R., "A Report on High Speed Wind Tunnel Testing of the Large Scale Advanced Prop-Fan," AIAA Paper 88-2802, July 1988.
- <sup>2</sup>Bober, L. J., Chaussee, D. S., and Kutler, P., "Prediction of High Speed Propeller Flow Fields Using a Three-Dimensional Euler Analysis," AIAA Paper 83-0188, Jan. 1983.
- <sup>3</sup>Denton, J. D., "Time Marching Methods for Turbomachinery Flow Calculations," *Numerical Methods in Applied Fluid Dynamics*, edited by B. Hunt, Academic Press, New York, 1980, pp. 473–493.
- <sup>4</sup>Pulliam, T. H., and Chaussee, D. S., "A Diagonal Form of an Implicit Approximate Factorization Algorithm," *Journal of Computational Physics*, Vol. 39, No. 2, Feb. 1981, pp. 347–363.
- <sup>5</sup>Barton, J. M., Yamamoto, O., and Bober, L. J., "Euler Analysis of Transonic Propeller Flows," *Journal of Propulsion and Power*, Vol. 3, No. 3, 1987, pp. 277–282.
- <sup>6</sup>Yamamoto, O., Barton, J. M., and Bober, L. J., "Improved Euler Analysis of Advanced Turboprop Propeller Flow," AIAA Paper 86-1521, June 1986.
- <sup>7</sup>Clark, B. J., and Scott, J. R., "Coupled Aerodynamic and Acoustical Predictions for Turboprops," NASA TM-87094, May 1986.
- <sup>8</sup>Nallasamy, M., Clark, B. J., and Groeneweg, J. F., "Euler Analysis of the Three-Dimensional Flow Field of a High Speed Propeller: Boundary Condition Effects," *Journal of Turbomachinery*, Vol. 109, No. 3, July 1987, pp. 332–339.
- <sup>9</sup>Bushnell, P., "Measurement of the Steady Surface Pressure Distributions on a Single Rotation Large Scale Advanced Prop-Fan Blade at Mach Numbers from 0.03–0.78," NASA CR-182124, July 1988.
- <sup>10</sup>Stefko, G. L., Rose, G. E., and Podboy, G. G., "Wind Tunnel Performance Results of an Aeroelastically Scaled 2/9 Model of the PTA Flight Test Prop-Fan," AIAA Paper 87-1893, July 1987.
- <sup>11</sup>Vaczy, C. M., and McCormick, D. C., "A Study of the Leading Edge Vortex and Tip Vortex on Propfan Blades," *Journal of Turbomachinery*, Vol. 109, No. 3, July 1987, pp. 325–331.
- <sup>12</sup>Rizzetta, D. P., and Shang, J. S., "Numerical Simulation of Leading-Edge Vortex Flows," *AIAA Journal*, Vol. 24, No. 2, 1986, pp. 237–245.